OUKA
The University of Osaka
Institutional Knowledge Archive

Title	Morphology prediction of elastically interacting Zr hydride precipitates and cracks in α -Zr using atomistically informed Eshelby's ellipsoidal inclusion
Author(s)	Ishii, Akio
Citation	Computational Materials Science. 2023, 231, p. 112568
Version Type	VoR
URL	https://hdl.handle.net/11094/92835
rights	This article is licensed under a Creative Commons Attribution-NonCommercial-NoDerivatives 4.0 International License.
Note	

The University of Osaka Institutional Knowledge Archive : OUKA

https://ir.library.osaka-u.ac.jp/

The University of Osaka

Computational Materials Science 231 (2024) 112568

Contents lists available at ScienceDirect

Computational Materials Science

journal homepage: www.elsevier.com/locate/commatsci

Full length article

Morphology prediction of elastically interacting Zr hydride precipitates and cracks in α-Zr using atomistically informed Eshelby's ellipsoidal inclusion

Akio Ishii

Department of Mechanical Science and Bioengineering, Osaka University, 1-3 Machikaneyama, Toyonaka, Osaka 560-8531, Japan

ARTICLE INFO

Keywords:
Zirconium alloys
Cracking
Eshelby's ellipsoidal inclusion
Atomistic simulation
Density functional theory

ABSTRACT

We propose an atomistically informed Eshelby's inclusion analysis to investigate the morphology of secondary phases, which elastically interacted with each other through their respective local strain fields. Using the proposed method, we predict the morphology of δ-hydride precipitates and cracks, which interacted in the α–Zr matrix. Planar cracks nucleate along the basal-normal δ-hydride disk. And at the crack tip, the prismatic-normal δ-hydride disk also nucleates depending on the stress condition around the crack, constructing the hydride-crack network. The findings contribute to the understanding of the fracture mechanism of Zr alloys, such as delayed hydride cracking, which is caused by Zr hydride.

1. Introduction

Zirconium alloys are commonly used as fuel cladding in nuclear reactors owing to their low cross-section for neutron absorption, good corrosion resistance, ductility, and fracture toughness. Because of environmental steam-water in nuclear reactors, hydrogen is generated from the surface oxidation of Zr fuel claddings. The generated hydrogen is then partly absorbed by the Zr fuel cladding and Zr hydride precipitates are produced once the hydrogen concentration in the Zr fuel cladding exceeds the limit of solid solubility [1,2]. Experimental studies have shown that Zr hydride precipitates negatively affect the mechanical properties of Zr alloys. For instance, the reduction in ductility and fracture toughness of Zr alloys due to Zr hydride precipitates has been experimentally observed [2–5].

Moreover, the morphology of Zr hydride precipitates and the interaction between the cracks and precipitates reportedly play an important role in the fracture of Zr alloys [1,2,6–10]. One of the famous phenomena related to this is the delayed hydride cracking (DHC). DHC is a slow fracture phenomena, such as conventional creep in high temperature, and the fracture is due to the slow progression of crack. Although the slow cracking may be due to the interacting nucleation of Zr hydride precipitates and the expansion of cracks around each other, the morphology of Zr hydride precipitates and cracks that interacted elastically through their respective local strain (or stress) fields [1,5] is still unclear, and theoretical analysis and computational simulations are necessary. However, computer simulations for the interaction between the Zr hydride precipitates and cracks are few [11] due to the challenging analysis and modeling of the crack in conventional simulation methods for the analysis of phase transitions. The crack nucleation and propagation are difficult to analyze using conventional atomistic simulations (e.g., molecular dynamics and density functional theory (DFT) calculations) because of the limitation in the temporal and spatial scales. Sophisticated modeling of the crack is still not achieved for phase field simulations, including the solid physics of the crack. Thus, present computational studies about DHC are usually focused on the hydrogen diffusion process, under finite element-based stress field around the crack tip [12–18]. Theoretical discussions of the morphology of interacting Zr hydride precipitates and cracks are few in our knowledge.

We previously proposed a parameter-free Eshelby's ellipsoidal inclusion analysis, which is atomistically informed using DFT calculation, and we successfully predicted the morphology of Zr hydride precipitates in α–Zr (hexagonal closed-packed structure) matrix and the morphology and stability of the B19' phase in B2 matrix for TiNi shape memory alloys [19–21]. As a subsequent work, we expand the applicability of our method and proposed an atomistically informed Eshelby's inclusion analysis to investigate the morphology of secondary phases or cracks under local strain fields caused by other existing phases or cracks. Using the proposed method, we predicted the morphology of Zr hydride precipitates and cracks, which interacted with each other in the α–Zr matrix. We predicted the morphology of the crack around the Zr hydride precipitate, i.e., under the strain field of Zr hydride precipitate.

E-mail address: ishii@me.es.osaka-u.ac.jp.

https://doi.org/10.1016/j.commatsci.2023.112568
Received 15 June 2023; Accepted 6 October 2023
0927-0256/© 2023 The Author(s). Published by Elsevier B.V. This is an open access article under the CC BY-NC-ND license (http://creativecommons.org/licenses/by-nc-nd/4.0/).

We have also predicted the morphology of the Zr hydride precipitate around the cracks; thus, drawing the whole picture of hydride-crack networks in Zr alloys.

2. Methodology

Micromechanics is a conventional analysis method for the local strain and stress field and elastic energy change caused by the distorted region in an elastic medium (referred to as the matrix in this study). The heterogeneous distortion is caused by the existence of the secondary phase, which has a different shape and thermal expansion from the matrix and is described in micromechanics using an eigenstrain distribution $\epsilon_{ij}(\boldsymbol{x})$ ($\boldsymbol{x} = [x_1; x_2; x_3]$ indicates a position inside the matrix). The eigenstrains indicate the *net* shape difference between the matrix and secondary phase, which excludes the effect of elastic distortion from the environment. Using the distribution of eigenstrains, $\epsilon_{ij}(\boldsymbol{x})$, for the case that the elastic constants of the matrix and secondary phase are same, we can calculate the distribution of the displacement $u_k(\boldsymbol{x})$ and total strains $\varepsilon_{kl}(\boldsymbol{x}) = \frac{1}{2}\left(\frac{\partial u_k}{\partial x_l} + \frac{\partial u_l}{\partial x_k}\right)$ by solving the following differential equation, described using the Einstein summation convention [22],

$$C_{ijkl}\frac{\partial^2 u_k(\boldsymbol{x})}{\partial x_l \partial x_j} = C_{ijkl}\frac{\partial \epsilon_{kl}(\boldsymbol{x})}{\partial x_j}, \tag{1}$$

where C_{ijkl} are elastic constants. The distribution of total strains is the actual strain distribution caused by the heterogeneous secondary phase, which includes the effect of both the shape difference between the matrix and secondary phase and the elastic distortion from the environment. Using the total strains ε_{kl}, the distribution of the internal stress $\sigma_{ij}(\boldsymbol{x})$ is derived as follows:

$$\sigma_{ij}(\boldsymbol{x}) = C_{ijkl}(\varepsilon_{kl}(\boldsymbol{x}) - \epsilon_{kl}(\boldsymbol{x})). \tag{2}$$

$(\varepsilon_{kl}(\boldsymbol{x}) - \epsilon_{kl}(\boldsymbol{x}))$ are the distribution of elastic strains, describing the elastic distortion from the environment.

Eshelby mentioned that the total strains and eigenstrains of the distorted region, $\varepsilon_{ij}^{\mathrm{inc}}$ and $\epsilon_{ij}^{\mathrm{inc}}$, are linearly connected with Eshelby's tensor, S_{klmn}, if we consider the distorted region and secondary phase, as an ellipsoidal inclusion ($\frac{x_1^2}{a_1^2} + \frac{x_2^2}{a_2^2} + \frac{x_3^2}{a_3^2} = 1$: a_i is the half axis of the ellipsoid in each direction) [23,24], and the eigenstrains are uniformly distributed in the inclusion,

$$\varepsilon_{kl}^{\mathrm{inc}} = S_{klmn}\epsilon_{mn}^{\mathrm{inc}}. \tag{3}$$

In the isotropic matrix, S_{klmn} depends only on Poisson's ratio and the shape of the ellipsoidal inclusion is independent of the volume. If the eigenstrains $\epsilon_{mn}^{\mathrm{inc}}$ and Eshelby's tensor S_{klmn} are known, the total strain $\varepsilon_{kl}^{\mathrm{inc}}$ and internal stress of the ellipsoidal inclusion $\sigma_{ij}^{\mathrm{inc}}$ are easily derived from Eqs. (2) and (3) *without* solving the differential Eq. (1). Using the derived $\sigma_{ij}^{\mathrm{inc}}$, the elastic energy increment ΔE (per unit volume of inclusion) owing to the inclusion in the matrix under external stress $\sigma_{ij}^{\mathrm{ex}}$ condition, is described as follows [22]:

$$\Delta E = -\frac{1}{2}\sigma_{ij}^{\mathrm{inc}}\epsilon_{ij}^{\mathrm{inc}} - \sigma_{ij}^{\mathrm{ex}}\epsilon_{ij}^{\mathrm{inc}}. \tag{4}$$

Comparing the elastic energy increment ΔE between the inclusions with different shapes and orientations, we can predict the stable shape and orientation as those of the inclusion with the minimum energy increment [19–21]. However, in the above equation, the external stress does not affect the morphology of the secondary phase; the $\sigma_{ij}^{\mathrm{ex}}$ term on the right-hand side only depends on the eigenstrains [19].

For the case that the elastic constants of the matrix, C_{ijkl}, and those of the inclusion (secondary phase), $\tilde{C}_{ijkl}$, are different, there is a relationship between the elastic constants of matrix C_{ijkl}, that of inclusion $\tilde{C}_{ijkl}$, and fictitious eigenstrains $\tilde{\epsilon}_{mn}$ based on Eshelby's "equivalent inclusion theory" for the ellipsoidal inclusion [22,24],

$$\tilde{C}_{ijkl}(S_{klmn}\tilde{\epsilon}_{mn} + \varepsilon_{kl}^{\mathrm{ex}} - \epsilon_{kl}^{\mathrm{inc}}) = C_{ijkl}(S_{klmn}\tilde{\epsilon}_{mn} + \varepsilon_{kl}^{\mathrm{ex}} - \tilde{\epsilon}_{kl}). \tag{5}$$

$\varepsilon_{kl}^{\mathrm{ex}}$ is the elastic strain of the matrix due to the external stress $\sigma_{ij}^{\mathrm{ex}}$. This equation describes replacing the inhomogeneity of the elastic constants by the extra eigenstrains. The left- and right-hand sides of this equation are derived from Eq. (2) for the real and fictitious inclusion, respectively, and the total strain term are described using fictitious eigenstrains $\tilde{\epsilon}_{mn}$ as $\varepsilon_{kl}^{\mathrm{inc}} = S_{klmn}\tilde{\epsilon}_{mn}$. Moreover, the equation also imply that micromechanics is applicable in calculating the local stress and strain and elastic energy change due to the existence of a void or crack under external stress $\sigma_{ij}^{\mathrm{ex}}$, considering the void or crack as ellipsoidal inclusions with inhomogeneous elastic constant $\tilde{C}_{ijkl} = 0$ [22]. Solving these simultaneous equations for $\tilde{\epsilon}_{mn}$ and calculating $\sigma_{ij}^{\mathrm{inc}}$ using Eq. (2), the elastic energy increment, $\Delta\tilde{E}$, owing to the inclusion in the matrix under external stress $\sigma_{ij}^{\mathrm{ex}}$ condition, is rewritten as follows [22]:

$$\Delta\tilde{E} = -\frac{1}{2}\sigma_{ij}^{\mathrm{inc}}\epsilon_{ij}^{\mathrm{inc}} - \sigma_{ij}^{\mathrm{ex}}\epsilon_{ij}^{\mathrm{inc}} - \frac{1}{2}\sigma_{ij}^{\mathrm{ex}}(\tilde{\epsilon}_{ij} - \epsilon_{ij}^{\mathrm{inc}}). \tag{6}$$

In contrast to Eq. (4), the third term on the right-hand side is a correlation term between the external stress and the shape and orientation of the inclusion because $\tilde{\epsilon}_{ij}$ are shape and orientation dependent. Furthermore, the external stress effect is also included in the first term ($\sigma_{ij}^{\mathrm{inc}}$) based on Eq. (5). Although the Eshelby's tensor conventionally applies for an isotropic matrix and inclusion, the general form of Eshelby's tensor for an anisotropic matrix and inclusion is also derived as follows based on the deduction of Kinoshita et al. [22,25]:

$$S_{klmn}^{*} = \frac{1}{8\pi}C_{pqmn}\int_{-1}^{1} d\zeta_3 \times \int_{0}^{2\pi}\left(\frac{\xi_l\xi_q N_{kp}(\xi_1,\xi_2,\xi_3) + \xi_k\xi_q N_{lp}(\xi_1,\xi_2,\xi_3)}{D(\xi_1,\xi_2,\xi_3)}\right) d\theta, \tag{7}$$

where

$$D(\xi_1,\xi_2,\xi_3) = P_{pqr}(C_{pj1l}\xi_j\xi_l)(C_{qm2n}\xi_m\xi_n)(C_{rs3t}\xi_s\xi_t),$$
$$N_{km}(\xi_1,\xi_2,\xi_3) = \frac{1}{2}P_{kst}P_{mnr}(C_{sjnl}\xi_l\xi_j)(C_{turv}\xi_u\xi_v),$$

which correspond to the determinant and cofactor of $K_{km} = C_{klmn}\xi_l\xi_n$, respectively. P_{pqr} denotes the permutation tensor. Using ζ_3 and θ, $\boldsymbol{\xi} = [\xi_1;\xi_2;\xi_3]$ are described as follows:

$$\begin{bmatrix}\xi_1\\ \xi_2\\ \xi_3\end{bmatrix} = \begin{bmatrix}\frac{\sqrt{1-\zeta_3^2}\cos\theta}{a_1}\\ \frac{\sqrt{1-\zeta_3^2}\sin\theta}{a_2}\\ \frac{\zeta_3}{a_3}\end{bmatrix}.$$

Mura et al. also demonstrated the calculation of the strain field around the ellipsoidal inclusion [26]. Following their derivation, the gradient of displacement $\frac{\partial u_i}{\partial x_j}$ at $\boldsymbol{x}$ due to the ellipsoidal inclusion with uniform eigenstrains can be described as follows,

$$\frac{\partial u_i}{\partial x_j}(\boldsymbol{x}) = C_{klmn}\tilde{\epsilon}_{mn}\int_{-1}^{1} d\zeta_3 \times \int_{0}^{2\pi}\left(\frac{\xi_j\xi_l N_{ik}(\xi_1,\xi_2,\xi_3)}{D(\xi_1,\xi_2,\xi_3)}\left(\frac{1}{4\pi}U(\boldsymbol{x}\cdot\boldsymbol{\xi} - 1) - \frac{1}{2\pi\tilde{x}}\delta(\boldsymbol{x}\cdot\boldsymbol{\xi} - 1)\right)\right) d\theta. \tag{8}$$

Here, $U(x)$ is a step function and $\delta(x)$ is a delta function, which is described as follows,

$$U(x) = \begin{cases}1 & (x \le 0)\\ 0 & (x > 0),\end{cases}$$

$$\delta(x) = \begin{cases}1 & (x = 0)\\ 0 & (\text{otherwise}),\end{cases}$$

limiting the range of the integration to $\boldsymbol{x}\cdot\boldsymbol{\xi} \le 1$ and $\boldsymbol{x}\cdot\boldsymbol{\xi} = 1$ for the first and second term on the right-hand side, and $\tilde{x} = \sqrt{(x_1/a_1)^2 + (x_2/a_2)^2 + (x_3/a_3)^2}$. Note that the center of the inclusion is at $\boldsymbol{x} = [0;0;0]$ in this equation. Using this equation and the relationship,

$$\epsilon_{ij}(\boldsymbol{x}) = \frac{1}{2}\left(\frac{\partial u_i}{\partial x_j} + \frac{\partial u_j}{\partial x_i}\right),$$

the distribution of the total strain is derived. Additionally, the stress distribution can be also derived using Eq. (2). The above equation gives $\epsilon_{ij}(\boldsymbol{x}) = \epsilon_{ij}^{\mathrm{inc}}$ for the position $\boldsymbol{x}$ inside the ellipsoidal inclusion because $\boldsymbol{x}$ is always satisfied $\boldsymbol{x} \cdot \boldsymbol{\xi} < 1$ during integration.

For the prediction of the hydride-crack interacted morphology, our scheme follows the above micromechanics theory, which regards the Zr hydride precipitates and cracks as ellipsoidal inclusions. Considering the inhomogeneity (between the α-Zr matrix and Zr hydride) and anisotropy of the elastic constants, using Eqs. (7), (5), and (6), we first calculated $\Delta\tilde{E}$ using numerically calculated S^*_{klmn} for the Zr hydride precipitate with different orientations and ellipsoid shapes and determined the most stable morphology by comparing the value of $\Delta\tilde{E}$. Using Eq. (8), we then numerically calculated the strain field around the Zr hydride precipitate for the determined morphology. The crack nucleation is then investigated around the Zr hydride precipitate, considering the calculated strain field of the precipitate as external stress $\epsilon_{ij}^{\mathrm{ex}}$ for the neighboring crack. We predicted the morphology of interacted crack by the strain field of neighboring Zr hydride precipitate by the method similar to that for the Zr hydride precipitate case. Then, we calculated the strain field around the crack, and determined the morphology of Zr hydride precipitate under the strain field of the crack by a similar calculation. Through this series of calculations, we predicted the morphology of the hydride-crack network, in which the nucleation of Zr hydride precipitates and cracks elastically interacted with each other.

For the detailed calculation setting, our targets are δ-hydride precipitates (face-centered tetragonal structure), which is the most frequently observed Zr hydride precipitate in experiments involving pure α–Zr matrix, and we focus on the prediction of the orientation for the Zr hydride because the shape of δ-hydride has been already specified as disk or plate-like experimentally and theoretically [1,19,27]. The crack was regarded as a needle or disk shape ellipsoidal inclusion to investigate its linear or planar nucleation, and it was considered as the inclusion with $\epsilon_{ij}^{\mathrm{inc}} = 0$ and $\tilde{C}_{ijkl} = 0$. Although the disk and needle are considered analytically as shapes with an extremely long and short half axes of inclusion (e.g., $a_1 = a_2$ and $a_3/a_1 \to 0$ for disk, $a_3/a_1 \to \infty$ for needle) [22,28], we consider $(a_1; a_2; a_3) = (20; 20; 1)$ and $(a_1; a_2; a_3) = (1; 1; 20)$ ellipsoid as disk and needle inclusions, respectively, because of the limitations of numerical calculations. For the orientation of disk and needle shape inclusions, we describe the elastic constants and eigenstrains in the coordinate system $\boldsymbol{x}'$ of the rotated disk and needle inclusions using the following rotation matrix

$$R_{ij} = \begin{bmatrix} \cos\psi & 0 & -\sin\psi \\ 0 & 1 & 0 \\ \sin\psi & 0 & \cos\psi \end{bmatrix} \times \begin{bmatrix} \cos\phi & \sin\phi & 0 \\ -\sin\phi & \cos\phi & 0 \\ 0 & 0 & 1 \end{bmatrix} = \begin{bmatrix} \cos\psi\cos\phi & \cos\psi\sin\phi & -\sin\psi \\ -\sin\phi & \cos\phi & 0 \\ \sin\psi\cos\phi & \sin\psi\sin\phi & \cos\psi \end{bmatrix}, \tag{9}$$

The normal direction of the disk plane and the longitudinal direction of the needle were set to $\boldsymbol{x}'_3$ [19,28]. We then calculated the orientation-dependent Eshelby's tensor and elastic energy increment by changing the rotation angle (ϕ, ψ) from 0° to 180° per 10°. The original coordinate system with $(\phi, \psi) = (0°, 0°)$ is set as $\boldsymbol{x}_1 - \boldsymbol{x}_2 - \boldsymbol{x}_3 = [0001]_{\alpha-\mathrm{Zr}}$–$[10\bar{1}0]_{\alpha-\mathrm{Zr}}$–$[1\bar{2}10]_{\alpha-\mathrm{Zr}}$. For the strain field calculation, as in Fig. 1, we only calculated the strain field in first quadrants by setting the center of the ellipsoidal inclusion at the origin of $\boldsymbol{x}'$ coordinate system and considering the symmetry of the ellipsoids. This is shown in plane I and II of Fig. 1. Note that determining a unit for the half axes is unnecessary because Eshelby's tensor is independent of the inclusion volume. Thus, the positions in this study are unitless. For the elastic constants of α-Zr and δ-hydride, we use the following values at Table 1. The values of eigenstrains for δ-hydride are, $\epsilon_{11}^{\mathrm{inc}} = 0.080$, $\epsilon_{22}^{\mathrm{inc}} = 0.062$, $\epsilon_{33}^{\mathrm{inc}} = 0.069$, $\epsilon_{12}^{\mathrm{inc}} = 0.166$ and $\epsilon_{23}^{\mathrm{inc}} = \epsilon_{31}^{\mathrm{inc}} = 0$, respectively. Note $\epsilon_{ij}^{\mathrm{inc}} = \epsilon_{ji}^{\mathrm{inc}}$. These values were obtained from our previous atomistic DFT calculations and thus a series of analysis in this study is atomistically informed and parameter-free [19].

Table 1
Elastic constants of α-Zr and δ-hydride calculated using the DFT calculation from Ref. [19]. Note that $C_{ijkl} = C_{jikl} = C_{ijlk} = C_{klij}$ and the values of other unlisted C_{ijkl} are zeros. The elastic constants are in GPa units. The coordinate system is $[0001]_{\alpha-\mathrm{Zr}}$–$[10\bar{1}0]_{\alpha-\mathrm{Zr}}$–$[1\bar{2}10]_{\alpha-\mathrm{Zr}}$.

	α-Zr	δ-hydride
C_{1111}	165	201
C_{2222}	149	191
C_{3333}	149	221
C_{1122}	70	108
C_{1133}	70	96
C_{2233}	65	100
C_{2323}	41	30
C_{3131}	27	22
C_{1212}	27	43
C_{1112}	0	−14
C_{2212}	0	−11
C_{3312}	0	11
C_{2331}	0	14

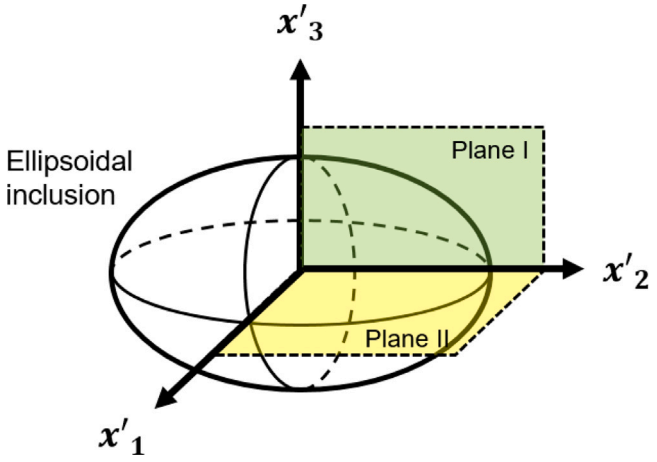

Fig. 1. The schematic of ellipsoidal inclusion at coordinate system $\boldsymbol{x}'_1 - \boldsymbol{x}'_2 - \boldsymbol{x}'_3$ for the calculation of strain fields. We only calculated the strain field on plane I and II in this study.

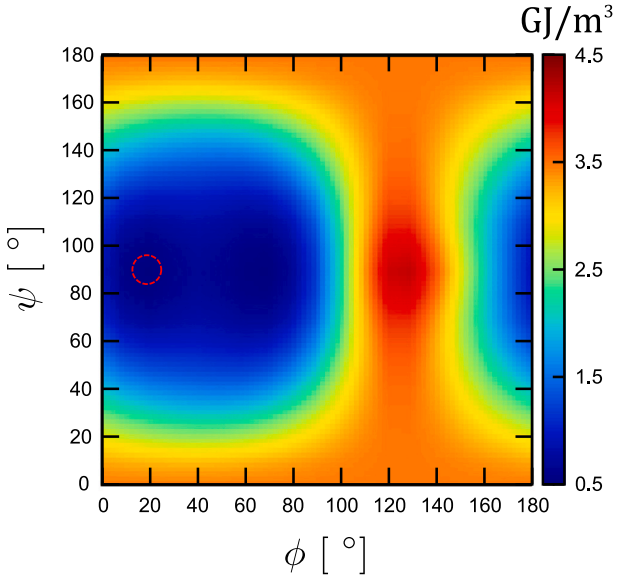

Fig. 2. Elastic energy increment $\Delta\tilde{E}$ change with respect to ϕ and ψ for the δ-hydride disk. Broken circle indicates the area with the minimum $\Delta\tilde{E}$.

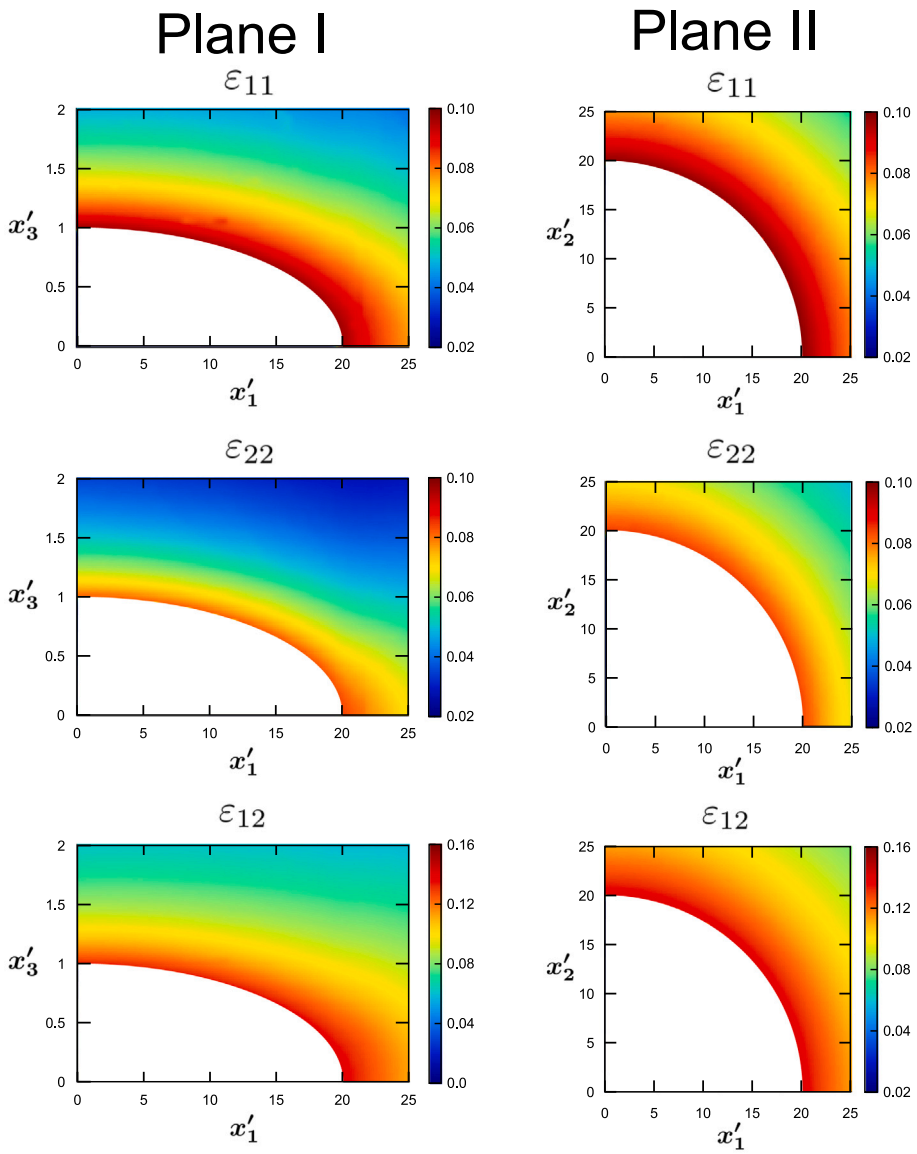

Fig. 3. Strain fields around $(\phi, \psi) = (20°, 90°)$ δ-hydride disk on plane I and II in Fig. 1. Note that all strain components are described in the original coordinate system $\boldsymbol{x}_1 - \boldsymbol{x}_2 - \boldsymbol{x}_3 = [0001]_{\alpha-Zr}$–$[10\bar{1}0]_{\alpha-Zr}$–$[1\bar{2}10]_{\alpha-Zr}$ and $\varepsilon_{33}(\boldsymbol{x}) = \varepsilon_{23}(\boldsymbol{x}) = \varepsilon_{31}(\boldsymbol{x}) = 0$. The strain fields inside the ellipsoid were omitted.

3. Results and discussion

In Fig. 2, we show the calculated $\Delta\tilde{E}(\phi, \psi)$ distribution. The minimum value of $\Delta\tilde{E}$ is at $(\phi, \psi) = (20°, 90°)$, corresponding to the basal-normal disk with small tilt (20°) about $\boldsymbol{x}_3$ $([1\bar{2}10]_{\alpha-Zr})$ axis. This is consistent with a previous experimental observation on a basal-normal planar micro-scale δ-hydride cluster with a small tilt [1]. For the δ-hydride disk with this orientation, we calculated the surrounding strain fields for each strain component, as shown in Fig. 3. Fig. 3 shows the distributions of the strain field on planes I and II (see Fig. 1) and we calculated the strain fields for 50 discrete positions at even intervals in the range from 0 to 25 for $\boldsymbol{x}'_1$ and $\boldsymbol{x}'_2$ and from 0 to 2 for $\boldsymbol{x}'_3$, followed by a linear interpolation. Around the δ-hydride disk, the large ε_{11}, ε_{22} and ε_{12} (in the original coordinate system $\boldsymbol{x}_1 - \boldsymbol{x}_2 - \boldsymbol{x}_3 = [0001]_{\alpha-Zr}$–$[10\bar{1}0]_{\alpha-Zr}$–$[1\bar{2}10]_{\alpha-Zr}$) are observed and these large strains will cause the crack. For instance, ε_{11} is 0.095 at the tip of the disk $(x'_1, x'_2, x'_3) = (21, 0, 0)$. This large strain is due to the large values of each eigenstrain component of δ-hydride and the compression to the δ-hydride disk from the matrix in basal plane due to the existence of $\epsilon^{\text{inc}}_{22}$ and $\epsilon^{\text{inc}}_{33}$. Furthermore, the existence of ε_{22} strain field is due to the tilt of the disk about the $\boldsymbol{x}_3$ $([1\bar{2}10]_{\alpha-Zr})$ axis; both ε_{22} and ε_{33} strain fields are zero if the δ-hydride disk is fully basal-normal: $(\phi, \psi) = (0°, 90°)$

A similar analysis was implemented to determine the morphology of the crack, considering the local strain at the tip of the δ-hydride disk, $(\boldsymbol{x}'_1, \boldsymbol{x}'_2, \boldsymbol{x}'_3) = (21, 0, 0)$, as external strain $\varepsilon^{\text{ex}}_{ij}$ for the crack around the δ-hydride disk. In Fig. 4, we show the calculated $\Delta\tilde{E}(\phi, \psi)$ distribution for (a) linear and (b) planar cracks. The minimum values of $\Delta\tilde{E}$ for linear and planar cracks are at $(\phi, \psi) = (0 - 180°, 0°)$ (basal-normal) and $(\phi, \psi) = (40°, 90°)$, respectively, and the lowest energy is at $(\phi, \psi) = (40°, 90°)$ for planar crack, corresponding to the basal-normal disk with the tilt 40° about $\boldsymbol{x}_3$ $([1\bar{2}10]_{\alpha-Zr})$ axis. Furthermore, not only at $(\phi, \psi) = (40°, 90°)$, $\Delta\tilde{E}$ values are relatively small at the region $(\phi, \psi) = (20 - 60°, 60 - 120°)$ for the planar crack. This means that planar cracks tend to nucleate along the above basal-normal δ-hydride disk. For the planar

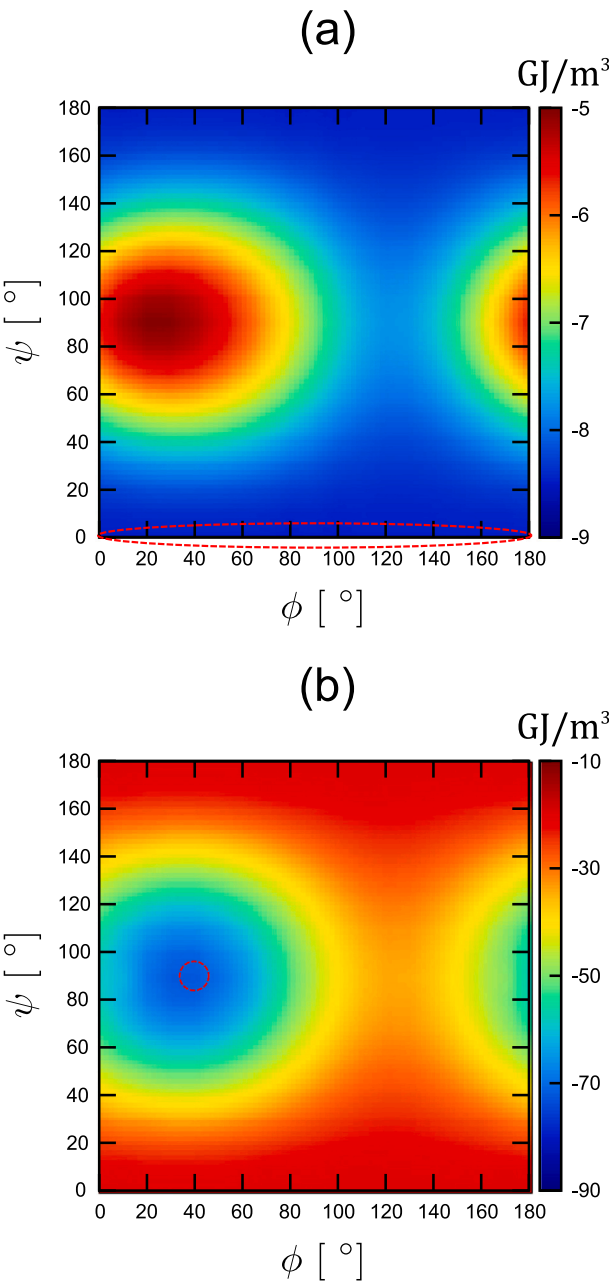

Fig. 4. Elastic energy increment $\Delta\tilde{E}$ change with respect to ϕ and ψ for the (a) linear and (b) planar cracks under the local strain field of δ-hydride disk. Broken ellipse and circle indicate the area with the minimum $\Delta\tilde{E}$.

crack with $(\phi, \psi) = (40°, 90°)$ orientation, we calculated the surrounding strain fields for each strain component, as shown in Fig. 5. Because the crack itself does not cause the strain field without external stress or strain, we apply the external strain, corresponding to external stress $\sigma_{11}^{ex} = 0.2$ GPa (basal-normal), $\sigma_{22}^{ex} = 0.2$ GPa, and $\sigma_{33}^{ex} = 0.2$ GPa (basal-parallel, corresponding to the circumferential tensile stress in experiment [7]), respectively. In Fig. 5, the calculated distributions of strain field at I and II planes under σ_{11}^{ex} and σ_{22}^{ex} are shown. The external stress σ_{11}^{ex} and σ_{22}^{ex} cause not only the normal strain, but also the shear strain component ε_{12} field from Fig. 5, and we confirmed that σ_{33}^{ex} does not generate the strain field. This is because the predicted basal-normal crack plane has a tilt about $\boldsymbol{x_3}$ $[1\bar{2}10]_{\alpha-Zr}$ but not about $\boldsymbol{x_2}$ $[10\bar{1}0]_{\alpha-Zr}$. Additionally, Eshelby's inclusion crack reproduced the well-known stress distribution of the crack in fracture mechanics, and the details are presented in the Appendix.

Using the calculated strain field at the tip of the planar crack, $(\boldsymbol{x}_1', \boldsymbol{x}_2', \boldsymbol{x}_3') = (21, 0, 0)$, for each external stress case, we recalculated the $\Delta\tilde{E}(\phi, \psi)$ distribution of δ-hydride disk to investigate the effect of strain field to the morphology of δ-hydride precipitates, predicting the morphology of δ-hydride precipitates at the nucleated crack tip. The calculated $\Delta\tilde{E}(\phi, \psi)$ distribution for the planar crack under (a) σ_{11}^{ex} and (b) σ_{22}^{ex} external stresses are shown in Fig. 6. Although $\Delta\tilde{E}$ distributions of both cases do not have a significant difference from that of the strain-free case in Fig. 2, the orientation of the minimum of $\Delta\tilde{E}$ changes from $(\phi, \psi) = (20°, 90°)$ to $(\phi, \psi) = (70°, 90°)$ for the σ_{22}^{ex} case, corresponding to the change in disk orientation from basal-normal to prismatic-normal. This is consistent with the experimental observation of the nucleation of δ-hydride disk normal to the crack line [1,7]. However, although the orientation of δ-hydride disk changes for the σ_{22}^{ex} case, the difference of $\Delta\tilde{E}$ value between $(\phi, \psi) = (20°, 90°)$ and $(\phi, \psi) = (70°, 90°)$ in strain-free distribution are originally not large; the value of $\Delta\tilde{E}$ is similarly low at the region $(\phi, \psi) = (0 - 80°, 90°)$ in Fig. 2; thus, our result supposes that the basal-normal δ-hydride disks will easily tilt about the $[1\bar{2}10]_{\alpha-Zr}$ direction originally, and the crack under certain stress condition, σ_{22}^{ex}, drives prismatic-normal disks more. Additionally, the morphology of the crack around $(\phi, \psi) = (70°, 90°)$ δ-hydride disk did not change.

4. Summary

In summary, we proposed a series of atomistically informed Eshelby's inclusion analysis to investigate the morphology of secondary phases, which interacted with each other elastically through their respective local strain fields in the matrix. Using the proposed method, we predicted the morphology of δ-hydrides and cracks, which interacted with each other in the α–Zr matrix. Planar cracks nucleate along the basal-normal δ-hydride disk. Moreover, at the crack tip, not only the basal-normal, the prismatic-normal δ-hydride disk also nucleates depending on the stress condition, constructing the hydride-crack network. Our findings contribute to the understanding of the fracture mechanism in Zr alloys, which was caused by Zr hydrides. Additionally, we should note that proposed analysis is also applicable other materials as well, e.g., crack-inclusion interaction in the steel or shape memory alloys [29,30].

Declaration of competing interest

The authors declare that they have no known competing financial interests or personal relationships that could have appeared to influence the work reported in this paper.

Data availability

Data will be made available on request.

Acknowledgments

This study was partially supported by JSPS KAKENHI, Japan Grant Number JP21K03771.

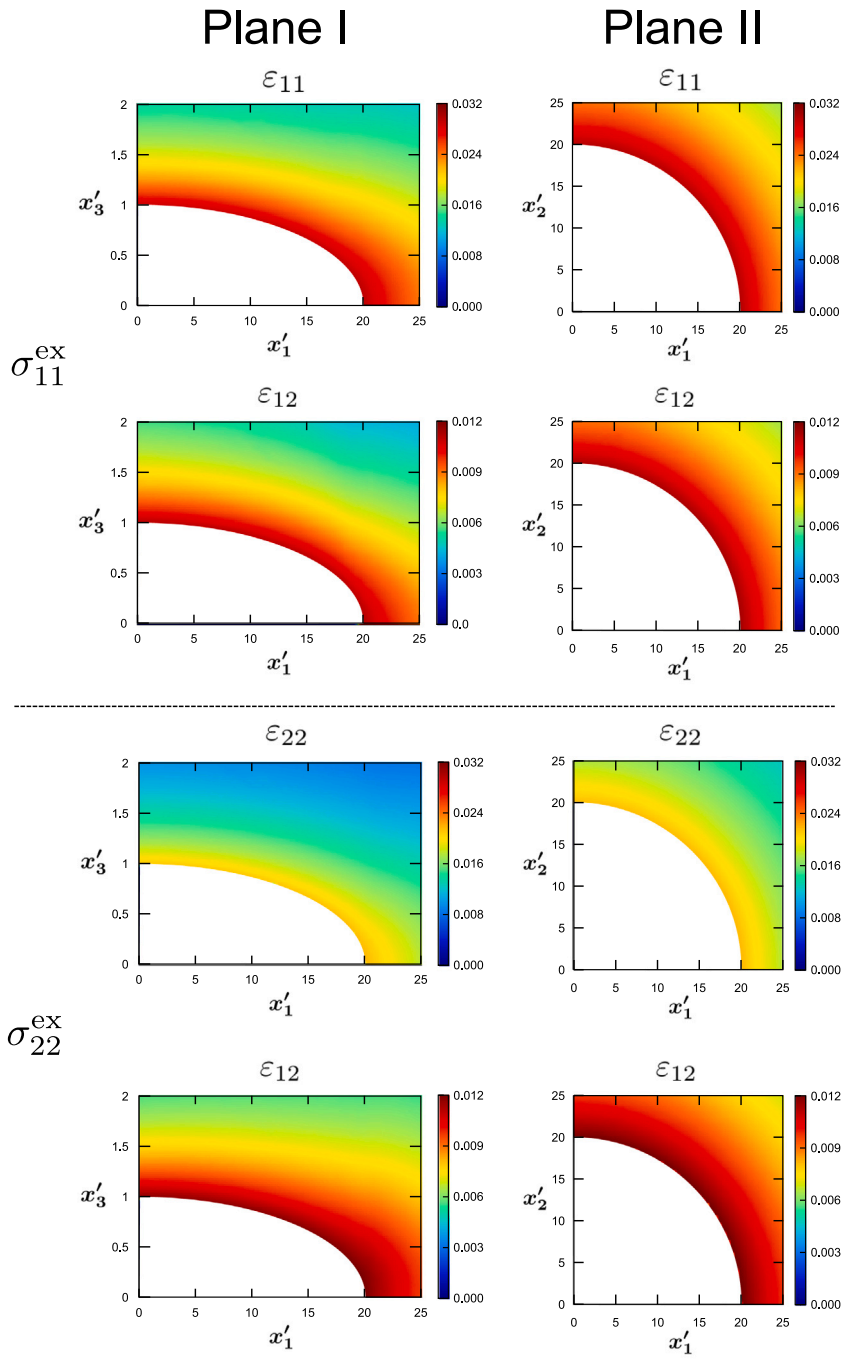

Fig. 5. Strain fields around $(\phi, \psi) = (40°, 90°)$ planar crack on planes I and II in Fig. 1 under $\sigma_{11}^{\mathrm{ex}} = 0.2$ and $\sigma_{22}^{\mathrm{ex}} = 0.2$ GPa condition. Note that all strain components are described in the original coordinate system $\boldsymbol{x}_1 - \boldsymbol{x}_2 - \boldsymbol{x}_3 = [0001]_{\alpha-Zr}$–$[10\bar{1}0]_{\alpha-Zr}$–$[1\bar{2}10]_{\alpha-Zr}$. $\varepsilon_{22}(\boldsymbol{x}) = \varepsilon_{33}(\boldsymbol{x}) = \varepsilon_{23}(\boldsymbol{x}) = \varepsilon_{31}(\boldsymbol{x}) = 0$ for $\sigma_{11}^{\mathrm{ex}}$, $\varepsilon_{11}(\boldsymbol{x}) = \varepsilon_{33}(\boldsymbol{x}) = \varepsilon_{23}(\boldsymbol{x}) = \varepsilon_{31}(\boldsymbol{x}) = 0$ for $\sigma_{22}^{\mathrm{ex}}$ and $\sigma_{33}^{\mathrm{ex}}$ did not cause the local strain field. The strain fields inside the ellipsoid were omitted.

Appendix

To confirm the reliability of the calculated strain field around the crack using Eshelby's ellipsoidal inclusion, we calculated the change of stress distribution along the crack tip for the isotropic matrix,

$$C_{ijkl} = \lambda\delta_{ij}\delta_{kl} + \mu(\delta_{ik}\delta_{jl} + \delta_{il}\delta_{jk}),$$

$\lambda = 60$ GPa, $\mu = 20$ GPa are used. $(a_1; a_2; a_3) = (10; 10; 1)$ ellipsoidal inclusion with $\tilde{C}_{ijkl} = 0$ (planar crack) in coordinate system $\boldsymbol{x_1} - \boldsymbol{x_2} - \boldsymbol{x_3}$ are used and $\sigma_{33}^{\mathrm{ex}} = 0.1$ GPa was applied. We then calculated the stress distribution along $\boldsymbol{x}_1$ direction from the crack tip and fit the values using the following function, which is the conventional form of the stress field around the crack tip in fracture mechanics [31],

$$\sigma(x) = \frac{K}{\sqrt{2\pi x}},$$

K is the stress intensity factor. The result is shown in Fig. 7. Although the fitted curve does not agree with the plots at the crack tip as the curve reaches infinity, the curve agrees well with the plots elsewhere,

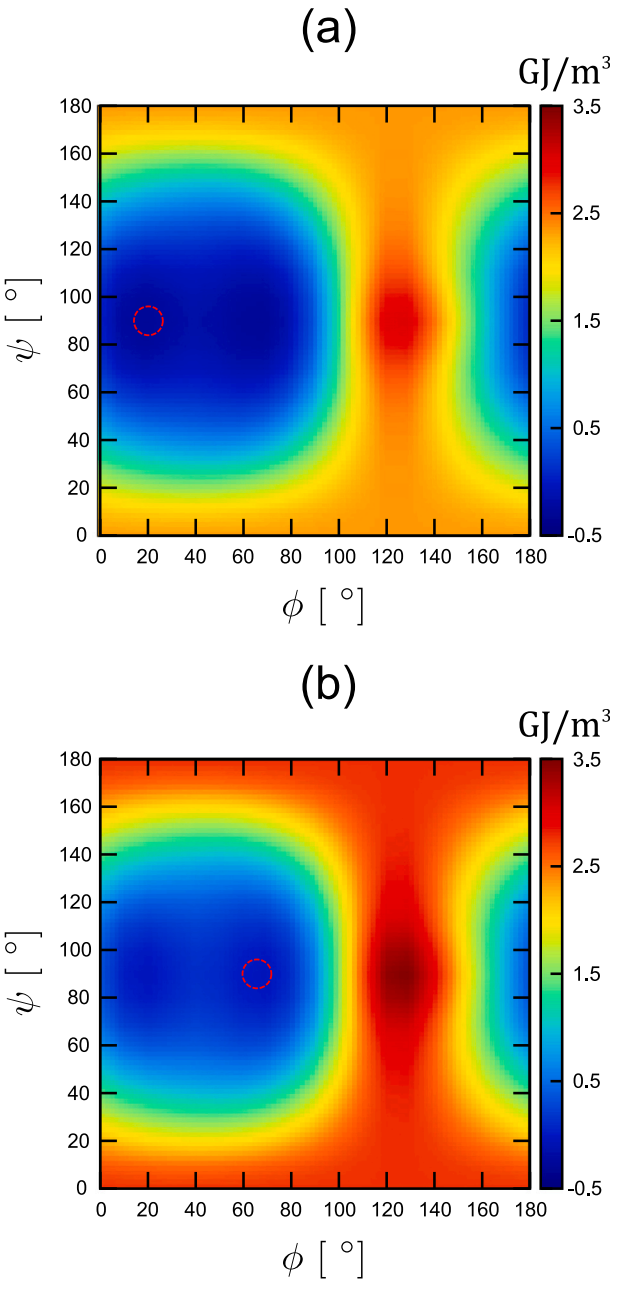

Fig. 6. Elastic energy increment $\Delta\tilde{E}$ change with respect to ϕ and ψ for δ-hydride disk under the local strain field of the crack: (a) $\sigma_{11}^{ex} = 0.2$ GPa (b) $\sigma_{22}^{ex} = 0.2$ GPa external stress condition. Broken circles indicate the area with the minimum $\Delta\tilde{E}$.

and the standard errors for the fitting are lower than 1% with fitted $K = 7.15$ GPa, confirming our result. Considering the effect of the crack tip curvature, the stress at the crack tip, σ_{33}^{tip}, is usually described as the following in fracture mechanics,

$$\sigma_{33}^{tip} = \sigma_{33}^{ex}\left(1 + 2\sqrt{\frac{a_1}{\rho}}\right),$$

ρ is the curvature radius at the crack tip. In our ellipsoid, using $\rho = a_3^2/a_1$ at the tip of the longitude of the ellipsoid, $\sigma_{33}^{tip} = 2.1$ GPa is estimated from this equation, which is consistent with the stress value at the crack tip in Fig. 7.

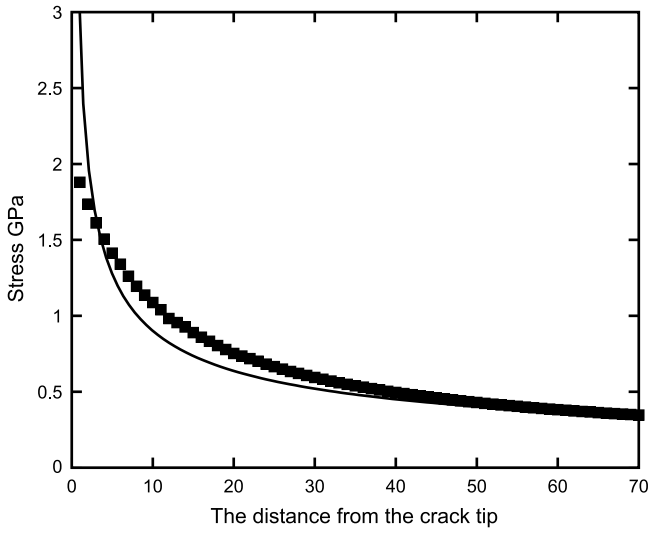

Fig. 7. σ_{33} plot along the x_1 direction from the tip of the ellipsoidal inclusion. The solid line is the fitted curve of $\sigma(x) = \frac{K}{\sqrt{2\pi x}}$.

References

[1] A.T. Motta, L. Capolungo, L.Q. Chen, M.N. Cinbiz, M.R. Daymond, D.A. Koss, E. Lacroix, G. Pastore, P.C.A. Simon, M.R. Tonks, B.D. Wirth, M.A. Zikry, Hydrogen in zirconium alloys: A review, J. Nucl. Mater. 518 (2019) 440–460.

[2] A.A. Plyasov, V.V. Novikov, Y.N. Devyatko, A review of hydride reorientation in Zirconium Alloys for water-cooled reactors, Phys. At. Nuclei 83 (2020) 1407–1424.

[3] D.O. Northwoodkosasih, Hydrides and delayed hydrogen cracking in zirconium and its alloys, Int. Met. Rev. 28 (1983) 92–121.

[4] C.E. Ells, Hydride precipitates in zirconium alloys (A review), J. Nucl. Mater. 28 (1968) 129–151.

[5] J. Bair, M. Asle Zaeem, M. Tonks, A review on hydride precipitation in zirconium alloys, J. Nucl. Mater. 466 (2015) 12–20.

[6] J.B. Bai, C. Prioul, D. François, Hydride embrittlement in ZIRCALOY-4 plate: Part I. Influence of microstructure on the hydride embrittlement in ZIRCALOY-4 at 20°C and 350°C, Metall. Mater. Trans. A 25 (1994) 1185–1197.

[7] S. Sagat, S. Shi, M. Puls, Crack initiation criterion at notches in Zr-2.5Nb alloys, Mater. Sci. Eng. A 176 (1994) 237–247.

[8] M. Le Saux, J. Besson, S. Carassou, C. Poussard, X. Averty, Behavior and failure of uniformly hydrided zircaloy-4 fuel claddings between 25°C and 480°C under various stress states, including RIA loading conditions, Eng. Fail. Anal. 17 (2010) 683–700.

[9] R.K. Sharma, S. Sunil, B. Kumawat, R. Singh, A. Tewari, B. Kashyap, Influence of hydride orientation on fracture toughness of CWSR zr-2.5 % nb pressure tube material between RT and 300°C, J. Nucl. Mater. 488 (2017) 231–244.

[10] R.K. Sharma, A. Bind, G. Avinash, R. Singh, A. Tewari, B. Kashyap, Effect of radial hydride fraction on fracture toughness of CWSR zr-2.5% Nb pressure tube material between ambient and 300°C temperatures, J. Nucl. Mater. 508 (2018) 546–555.

[11] X.H. Guo, S.Q. Shi, Q.M. Zhang, X.Q. Ma, An elastoplastic phase-field model for the evolution of hydride precipitation in zirconium. Part II: Specimen with flaws, J. Nucl. Mater. 378 (2008) 120–125.

[12] G.A. McRae, C.E. Coleman, B.W. Leitch, The first step for delayed hydride cracking in zirconium alloys, J. Nucl. Mater. 396 (2010) 130–143.

[13] P.F. Weck, E. Kim, V. Tikare, J.A. Mitchell, Mechanical properties of zirconium alloys and zirconium hydrides predicted from density functional perturbation theory, Dalton Trans. 44 (2015) 18769–18779.

[14] Y. Zhang, X.M. Bai, J. Yu, M.R. Tonks, M.J. Noordhoek, S.R. Phillpot, Homogeneous hydride formation path in α-Zr: Molecular dynamics simulations with the charge-optimized many-body potential, Acta Mater. 111 (2016) 357–365.

[15] Z. Xia, J. Zhang, Q. Tong, S. Ding, Multi-physics modeling of delayed hydride cracking in zirconium alloys, J. Mech. Phys. Solids 132 (2019) 103677.

[16] Z. Xia, B. Wang, J. Zhang, S. Ding, L. Chen, H. Pang, X. Song, Three-dimensional numerical simulation of hydrogen-induced multi-field coupling behavior in cracked zircaloy cladding tubes, Nucl. Eng. Technol. 51 (2019) 238–248.

[17] H. Abdolvand, Progressive modelling and experimentation of hydrogen diffusion and precipitation in anisotropic polycrystals, Int. J. Plast. 116 (2019) 39–61.

[18] A. Tondro, H. Abdolvand, Quantifying hydrogen concentration in the vicinity of zirconium hydrides and deformation twins, J. Mech. Phys. Solids 148 (2021) 104287.

[19] A. Ishii, *Ab* Initio morphology prediction of Zr hydride precipitates using atomistically informed Eshelby's ellipsoidal inclusion, Comput. Mater. Sci. 211 (2022) 111500.
[20] A. Ishii, Elastic investigation for the existence of B33 phase in TiNi shape memory alloys using atomistically informed Eshelby's ellipsoidal inclusion, Comput. Mater. Sci. 218 (2023) 111954.
[21] A. Ishii, Ab initio prediction of temperature-dependent stability of heterogeneous B19' phase in TiNi alloy using atomistically informed Eshelby's ellipsoidal inclusion, Mater. Today Commun. 35 (2023) 105861.
[22] T. Mura, Micromechanics of Defects in Solids, Springer Science & Business Media, 2013.
[23] J.D. Eshelby, The determination of the elastic field of an ellipsoidal inclusion, and related problems, Proc. R. Soc. Lond. Ser. A 241 (1957) 376–396.
[24] J.D. Eshelby, Elastic inclusions and inhomogeneities, Prog. Solid Mech. 2 (1961) 89–140.
[25] N. Kinoshita, T. Mura, Elastic fields of inclusions in anisotropic media, Phys. Stat. Solidi (A) 5 (1971) 759–768.
[26] T. Mura, P.C. Cheng, The elastic field outside an ellipsoidal inclusion, J. Appl. Mech. 44 (1977) 591–594.
[27] G. Han, Y. Zhao, C. Zhou, D.-Y. Lin, X. Zhu, J. Zhang, S. Hu, H. Song, Phase-field modeling of stacking structure formation and transition of δ-hydride precipitates in zirconium, Acta Mater. 165 (2019) 528–546.
[28] M. Kato, T. Fujii, S. Onaka, Elastic strain energies of sphere, plate and needle inclusions, Mater. Sci. Eng. A 211 (1996) 95–103.
[29] H. Atkinson, G. Shi, Characterization of inclusions in clean steels: a review including the statistics of extremes methods, Prog. Mater. Sci. 48 (2003) 457–520.
[30] S. Yi, S. Gao, L. Shen, Fracture toughening mechanism of shape memory alloys under mixed-mode loading due to martensite transformation, Int. J. Solid Stress. 38 (2001) 4463–4476.
[31] G. Chell, Developments in Fracture Mechanics. Vol. 1, Applied Science Publishers, 1979.